YTUP

Journal of Thermal Engineering
https://jten.yildiz.edu.tr/
https://doi.org/10.47481/jten.0051

RESEARCH ARTICLE

Pool boiling heat transfer enhancement using nanofluids on structured surfaces

Suryaji S. Kale[1,*], Sonal S. More[2], M. B. Kulkarni[3], B. R. Birajdar[4], A. S. Dhobale[5], K. A. Shaikh[6]

[1]Assistant Professor, Department of Mechanical Engineering, N. K. Orchid College of Eng. & Tech., Solapur, DBATU University, Gat No.16, Solapur-Tuljapur Road, Near Mashroom Ganapati Temple, Solapur, 413002, Maharashtra, India
[2]Assistant Professor, Department of Electronic and Telecommunication Engineering, N. K. Orchid College of Eng. & Tech. Solapur, DBATU University, Gat No.16, Solapur-Tuljapur Road, Near Mashroom Ganapati Temple, Solapur, 413002, Maharashtra, India
[3]Assistant Professor, Department of Mechanical Engineering, N. K. Orchid College of Eng. & Tech., Solapur, DBATU University, Gat No.16, Solapur-Tuljapur Road, Near Mashroom Ganapati Temple, Solapur-413002, Maharashtra, India
[4]Assistant Professor, Department of Mechanical Engineering, N. K. Orchid College of Eng. & Tech., Solapur, DBATU University, Gat No.16, Solapur-Tuljapur Road, Near Mashroom Ganapati Temple, Solapur, 413002, Maharashtra, India
[5]Assistant Professor, Department of Mechanical Engineering, N. K. Orchid College of Eng. & Tech., Solapur, DBATU University, Gat No.16, Solapur-Tuljapur Road, Near Mashroom Ganapati Temple, Solapur, 413002, Maharashtra, India
[6]Assistant Professor, Department of Mechanical Engineering, N. K. Orchid College of Eng. & Tech., Solapur, DBATU University, Gat No.16, Solapur-Tuljapur Road, Near Mashroom Ganapati Temple, Solapur, 413002, Maharashtra, India

Abstract

Improvement in heat-transfer performance is a major requirement in contemporary thermal management systems, particularly in high-heat-flux applications. The application of nanofluids combined with surface modification methods has emerged as a viable measure to counter the shortcomings of traditional heat-transfer fluids. This study experimentally investigates the effects of nanoparticle concentration and surface geometry on convective heat-transfer characteristics. Graphene nanofluids with three volume fractions (0.2, 0.5, and 1) were prepared, and experiments were conducted on plain, V-structured, and square-structured surfaces. Thermal transfer properties were measured at heat inputs of 56 W, 72 W, and 90 W. The results show that the volume fraction of nanoparticles in the suspension always increases with the heat transfer coefficient, irrespective of surface arrangement. The heat transfer coefficient was also high for heat input at a given volume fraction. Structured surfaces exhibited substantially better thermal performance than plain surfaces because they more effectively disrupted the thermal boundary layer and induced greater flow disturbance. The heat transfer coefficient of the plain surface at a nanoparticle volume fraction of 1 percent and a heat input of 90 W was 28.19 W/m^{2o}C, the V-structured and square-structured surfaces recorded 36.145 W/m^{2o}C and 52.21 W/m^{2o}C, respectively. This corresponds to heat transfer improvements of 28.2% and 85.20% on the V-structured and square-structured surfaces, respectively, compared with the plain surface. The research proves that the hybrid application of graphene-based nanofluids and surface structuring significantly enhances the heat-transfer performance and that surface structuring with the square form is most promising for high-end thermal-performance applications. The novelty of the present work lies in experimentally comparing pool-boiling heat-transfer performance of graphene nanofluids on plain, V-grooved, and square-structured heating surfaces under identical test conditions, thereby highlighting the influence of simple, manufacturable surface geometries on boiling enhancement.

Keywords: Pool boiling, structured surfaces, graphene nanoparticles, nanofluids, enhancement in heat transfer coefficient

Cite this article as: Kale, S. S., More, S. S., Kulkarni, M. B., Birajdar, B. R., Dhobale, A. S., & Shaikh, K. A. (2026). Pool boiling heat transfer enhancement using nanofluids on structured surfaces. Journal of Thermal Engineering, 12(5), 1588–1610. https://doi.org/10.47481/jten.0051

1. Introduction

Effective boiling heat transfer is required in most thermal applications, such as power generation, refrigeration, electronic cooling, and small heat exchangers, because nucleate boiling can enable the removal of extremely high heat fluxes with only small wall-superheat requirements. However, the availability of stable nucleation sites, bubble departure and rewetting processes, and surface dry-out under increasing heat flux often limit practical boiling performance. Therefore, two of the most

*Corresponding Author
E-mail Adress: kalesss@gmail.com

Submitted: 11 January 2026; **Accepted:** 17 March 2026

This paper was recommended for publication in revised form by Editor-in-Chief Ahmet Selim Dalkılıç

common approaches to enhance performance are: (i) the use of nanoparticle suspensions (nanofluids) to improve the thermophysical properties of the working fluid; and (ii) the design of the heater surface (roughness, structures, and wettability patterns) to facilitate nucleation without hindering liquid replenishment.

Nanofluids were initially proposed to improve heat transfer by increasing effective thermal conductivity and altering near-wall transport behavior. Initial experiments indicated a significant conductivity increase in nanoparticle-dispersed base fluids, which stimulated many studies in the field of convective and boiling heat transfer applications [13]. Subsequent experimental studies in laminar flow and tube convection also demonstrated that the loading of nanoparticles could change the heat transfer coefficients with respect to concentration, stability, and flow/thermal boundary development [3,5]. Other characteristics that were also emphasized in review articles included that, in addition to conductivity, particle aggregation, interfacial resistance and dispersion stability are highly influential in overall thermal advantage [4]. The results show that nanofluids may be promising, but improved performance is not guaranteed and must be validated experimentally under the conditions in which the nanofluids will be used.

Graphene and graphene-based materials have received particular attention among other sophisticated nanoparticles due to their remarkable intrinsic thermal performance, as well as high aspect ratio [8]. It has been experimentally and analytically demonstrated that graphene can offer significant thermal transport enhancement in base fluids at relatively low loading in cases where dispersion is stable [6,7]. Indicatively, nanofluids made out of graphene have been reported to exhibit enhanced thermal/ electrical property and quantifiable increase in convective heat transfer in specific regimes [6,9]. Graphene nanosheets in ethylene glycol have also shown significant improvement on thermal conductivity with increasing volume fraction, with 2D morphology and interfacial effect being important ones [7]. Taken together, these reports indicate that graphene-based nanofluids could be promising candidates for improving boiling heat transfer provided that the formulation procedure yields stable, reproducible suspensions.

At the same time, surface treatment has been shown to be an effective method for intensifying boiling. Classical boiling theory and subsequent mechanistic theories highlight that surface wettability and geometry govern the behavior of bubble nucleation, growth and departure and critical heat flux (CHF) [11]. Recent micro/nano-fabrication research also indicates that structured surfaces(microcavities, porous layers, hybrid wettability patterns)can both enhance the heat transfer coefficient (HTC) in nucleate boiling and retard dry-out by improving capillary rewetting and supplying liquid [12-15]. As an example, the concept of mixed wettability(biophilic)has demonstrated that the combination of hydrophilic and hydrophobic groups can enhance nucleation and at the same time enable the stable replenishment of the liquid [12,13]. The detailed reviews also conclude that phase-change heat transfer through surface engineering is best when it achieves a balance between nucleation activation and constant rewetting as opposed to maximizing either of the two [14]. Recent experiments of multiscale textured metallic surfaces show huge increases of HTC and CHF because of the increase of nucleation site density and strong wicking behavior [15]. Extreme boiling is also demonstrated on laser-controlled microcavity and micro/nano-hierarchical surfaces by controlling cavity size scales and surface chemistry [16].

Despite studies of both graphene nanofluids and structured boiling surfaces, there remains a practical need to compare simple, manufacturable structured geometries under controlled heat input while systematically varying the graphene volume fraction. Specifically, repeatable macro- and microstructure heater plates (including V-groove and square-pattern textures) are more readily produced in many laboratories than more complicated microfabricated arrays; however, comparative results at several nanoparticle loadings and under the same test conditions remain scarce. Furthermore, one should determine not only whether the increase is caused by HTC but also which surface geometry provides the optimal increase for a given nanoparticle volume fraction and within a given range of heat input.

In this work, three nanoparticle volume fractions (0.2 vol%, 0.5 vol%, and 1.0 vol%) of graphene-based nanofluids were prepared using a controlled preparation route and characterized using FT-IR/XRD/SEM/Raman/UV-Vis, as applicable. An in-house experimental pool-boiling apparatus was designed and fabricated to measure three heater surface structures—plain, V-structured, and square-structured—under the same conditions. Boiling tests were conducted at electrical heat inputs (representative levels in the study: 56 W, 72 W, and 90 W), and the heat fluxes and heat transfer coefficients for each surface-fluid combination were measured. Thus, the study will provide a direct experimental comparison of (i) nanoparticle volume fraction, (ii) surface geometry, and (iii) the combined effect of structured surfaces and graphene loading on boiling heat transfer performance. Depending on the trends measured, the most successful surface geometry is selected in the tested heat-input range, and practical observations that concern boiling behavior (bubble activity, coalescence tendency and behavior of rewetting surface) are presented in accordance with known boiling enhancement mechanisms [11-15].

Du et al. [52] investigated the pool boiling performance of Fe_3O_4 nanofluids and observed that nanoparticle deposition on the heating surface significantly enhanced nucleate boiling heat transfer. The study reported improved heat transfer coefficient and delayed critical heat flux due to increase surface roughness and nucleation site density.

Freitas et al. [53] examined the pool boiling of nanofluids on biophilic surfaces and found that the pattern of surface wettability had a significant effect on the pattern of bubble nucleation and bubble growth. Their findings revealed improved heat-transfer perfor-

mance due to increased bubble-departure frequency and controlled nucleation behavior.

Moghadam et al. [54] experimentally studied the grooved surfaces using hybrid graphene oxide-iron oxide nanofluids. The findings showed a substantial increase in the heat transfer coefficient due to the nanofluid's superior thermal conductivity and the greater number of nucleation sites provided by the structured surface.

Pereira et al. [55] conducted a review of different methods of improving pool boiling heat transfer, such as the application of nanofluids and micro/nano-structured surfaces. In their research, they emphasized that surface modification and nanoparticle suspension can play a decisive role in improving the boiling performance by enhancing the number of nucleation sites and the dynamics of the bubbles.

Ullah et al. [56] indicated that micro- and nano-structured surfaces were capable of greatly increasing the pool boiling heat transfer through the promotion of early bubble nucleation and enhancing the replenishment of the liquid to the heated surface. They also found that surface geometry plays a significant role in bubble growth and separation.

Abdelrashied et al. [57] studied the effect of nanoparticles and surfactants on the nucleation of pool boiling heat transfer. The findings showed that nanoparticles increased thermal conductivity and facilitated bubble nucleation, thereby increasing the boiling heat transfer coefficient.

Gupta et al. [58] carried out experimental studies on hybrid nanofluids in structured microchannels and achieved an improvement in boiling heat transfer performance. This enhancement was largely explained by enhancements in turbulence, thermal conductivity, and bubble-formation properties.

Fadhl [59] studied the impact of CuO nanofluids on fin-structured heating surfaces and found that there was an evident increase in boiling heat transfer performance. This research has led to the conclusion that structured surfaces, when used with nanofluids, can greatly enhance nucleation-site density and heat-transfer efficiency.

Kuberan and Gedupudi [60] examined the nucleate pool boiling on micro-structured surfaces and came up with predictive models to estimate the boiling heat transfer characteristics. Their research demonstrated the significance of surface geometry and fluid properties for boiling heat-transfer performance.

Sotoudeh and Ghazanfarian [61] examined how wettability of surfaces in boiling pools can influence the heat transfer rate in boiling pools using molecular dynamics simulations. Their findings showed that hydrophilic surfaces enhance nucleation and heat-transfer performance owing to improved liquid-surface interaction.

To evaluate the performance of the proposed structured surfaces and graphene nanofluids, the experimental results obtained were compared with trends reported in previous pool-boiling studies. The results indicate that structured surfaces, combined with graphene nanofluids, lead to a noticeable improvement in heat transfer performance compared with plain surfaces. Similar enhancement trends have been reported in earlier investigations, in which surface structuring and nanofluids increased nucleation site density and improved boiling heat transfer characteristics.

The present work focuses primarily on enhancing pool-boiling heat-transfer performance and increasing the heat transfer coefficient by employing different surface geometries. Although the experimental observations provide insight into the boiling behavior at higher heat-flux conditions, a detailed investigation of the critical heat flux (CHF)was not the primary objective of this study. Therefore, CHF behavior is discussed only within the constraints of experimental observations.

Despite significant research on pool boiling heat transfer enhancement using nanofluids and structured surfaces, most existing studies focus either on improving the thermophysical properties of nanofluids or on employing complex micro- or nano-structured surfaces fabricated using advanced techniques. Although such approaches demonstrate improved boiling performance, their practical application is often limited due to manufacturing complexity, high fabrication costs, and the lack of systematic comparisons under identical experimental conditions.

Moreover, a limited number of experimental investigations have reported the combined effect of nanofluids and simple, macro-structured heating surfaces that can be easily manufactured and implemented in practical thermal systems. Comparative studies of plain, V-grooved, and square-structured surfaces with graphene nanofluids under identical pool-boiling conditions are rare in the literature.

Therefore, the present study experimentally investigates the pool-boiling heat-transfer performance of graphene nanofluids on three heating surfaces: plain, V-grooved, and square-structured. What is novel in this work is the systematic comparison of these simple, manufacturable surface structures under the same operating condition to determine their effects on heat transfer enhancement and boiling behavior.

This study presents an experimental investigation of pool boiling heat transfer in graphene nanofluids. Three heating surfaces - plain, V-grooved, and square-structured - were designed and tested in this study to determine their impact on boiling performance. These surfaces were systematically compared by keeping all the experimental conditions the same to be able to have a credible determination of the heat transfer properties. The experiment also determines the impact of surface structure on the heat flux and the overall improvement of boiling heat transfer, thus providing informative insights

into the contribution of simple, easy to fabricate surface geometries to the performance of pool boiling.

2. Methodology

In the current piece, the authors have used an experimental method to investigate the synergistic effect of the nanoparticle volume fraction and surface geometry on the performance of boiling heat transfer. In the research work, steps have been adhered to.

2.1. Nanofluids preparation and characterization

Graphene nanofluids were prepared by the two-step method at volume fractions of 0.2%, 0.5%, and 1%. Graphene nanoparticles were added to the base fluid in the required amount and subjected to mechanical stirring; this initial mixing was followed by ultrasonication to obtain stable, uniform suspensions. The structural and morphological details of the nanoparticles and nanofluids were verified by FT-IR, XRD, SEM, Raman spectroscopy, and UV-Visible spectroscopy. The process of heater-surface fabrication involves producing heater surfaces deposited onto a carrier to form a heater-surface assembly.

2.2. Heater surface fabrication process

The heater-surface fabrication process involved depositing the heater surface onto a carrier, forming a complete heater-surface assembly. Various surface configurations of the heater - plain, V-structured, and square-structured - were produced using conventional machining methods. Copper was chosen as the base material for all heater surfaces. All fabricated surfaces were thoroughly cleaned before the experiments so that surface conditions during experimentation were equivalent.

2.3. The experimental set up and procedure

An experimental setup was designed, constructed, and tested for pool boiling. A regulated power source was used to provide electrical heating to the heating surfaces rated at 56 W, 72 W, and 90 W. Surface and bulk fluid temperatures were measured using calibrated thermocouples. Each surface configuration and each nanofluid volume fraction were tested once the steady-state conditions were reached.

2.4. Data reduction and analysis

The heat transfer coefficient and the heat flux were determined using standard heat transfer relations based on the available heat input, the effective heat transfer area, and the temperature difference between the heating surface and the bulk fluid. Structured surfaces were also compared with the plain surface, and the percentage improvement in the heat transfer coefficient was determined under the same operating conditions.

3. Preparation, synthesis and characterization of nanofluids

To develop advanced nanofluids, the nanomaterials used to create nano-additives are highly diverse, including metallic, organic, and inorganic types. Figure 1 provides a schematic diagram of the procedures for producing nano fluids and nano-lubricants, their characterization methods, and their main properties. Among the many nanomaterials studied, carbon-based nanostructures are among the most promising because of their high-performance properties.

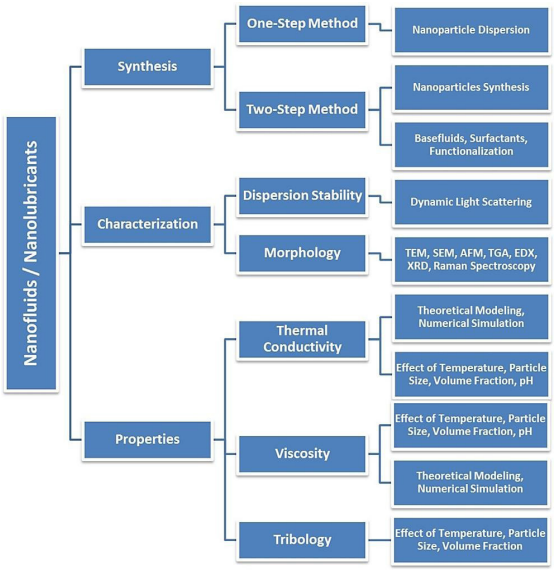

Figure 1. Schematic overview of nanofluids/nano lubricants: synthesis, characterization, and properties

Graphene is the best allotrope of carbon due to its high mechanical strength, structural integrity, and high thermal and electrical conductivity. Since its successful isolation in 2004 by Novoselov et al., graphene has received much scientific and industrial attention. Graphene is an atomic layer of carbon atoms arranged in a two-dimensional (honeycomb) lattice, with the atoms sp2-hybridized.

In practice, graphene is typically fabricated by multilayer stacking comprising over ten layers, which are commonly known as graphene nanoplatelets or graphene nanosheets (GnPs). These nanoplatelets combine the unique properties of single-layer graphene with the advantages of highly ordered graphitic carbon. Therefore, the thermal conductivity of graphene nanoplatelets is an order of magnitude greater than that of other allotropes of carbon, including single-walled carbon nanotubes (SWNTs), multi-walled carbon nanotubes (MWNTs), and diamond.

Another important property of graphene nanosheets is their high specific surface area, which is greater than that of nanotubes and most conventional nanoparticles. This increase in surface area enhances the interfacial contact between the nanoplatelets and the underlying fluid, thereby increasing heat transfer. Such efficient contact can reduce the Kapitza (interfacial thermal) resistance at the

solid-fluid interface and thereby facilitate a significant increase in the nanofluid's thermal conductivity.

In addition to their excellent thermal properties, graphene-based nanomaterials are amenable to relatively straightforward and affordable mass production. This qualifies them well for the development of next-generation nanofluids with improved thermal performance. Nevertheless, one of the biggest shortcomings of graphene is that it is highly hydrophobic, which prevents its dispersion in water and most polar organic solvents over a prolonged period and generally leads to particle agglomeration.

To address this challenge, the dispersibility of graphene nanosheets can be increased by modifying the interactions between the nanosheets and the surrounding fluid. This may be achieved by non-covalent functionalization using surfactants or by covalent functionalization via incorporation of hydrophobic or hydrophilic functional groups at high-energy sites on the graphene surface. Table 1 summarizes the specifications of the graphene nanoparticles used in this study.

Table 1. Specification of graphene nanoparticle

Parameters	Values
Purity	>99%
Thickness	15-20nm
Length	5-10 micron
No. of layers	4-8 (average)
Surface area	190 m^2/g
Density	1500 kg/m^3
Thermal conductivity	3000 w/mk
Tensile modulus	>1000Gpa
Electrical conductivity	10^7 simens/m
Physical form	Fluffy, very light powder
Color	Grey black

3.1. Mass of Nanoparticles

$$A = \frac{(\frac{m_P}{\rho_P})}{(\frac{m_P}{\rho_P} + V_{BF})} \times 100 \quad (1)$$

ϕ = volume concentration, %

mp = mass of nanoparticles, kg

ρ = density of nanoparticles, kg/m^3

VBF = volume of base fluid, m^3

Iteration I: For Volume fraction (ϕ) = 0.2% volume

Total volume of base fluid = 6 liters

Deionized water (DI-70%) = 4.2 liters

Ethylene Glycol (EG-30%) = 1.8 liters

Mass of Graphene = 9.009gms

SDBS = 0.9009gms (10% of mp)

Ammonium hydroxide = 30 ml (5% of VBF)

Iteration II: For Volume fraction (ϕ) = 0.5% vol

Total volume of base fluid = 6 liters

Deionized water (DI-70%) = 4.2 liters

Ethylene Glycol (EG-30%) =1.8 liters

Mass of Graphene = 45.22 gms

SDBS = 4.522gms (10% of Ammonium hydroxide)

= 30 ml (5% of VBF)

Iteration III: For Volume fraction (ϕ)= 1% vol

Total volume of base fluid = 6 liters

Deionized water (DI-70%) = 4.2 liters Ethylene

Glycol (EG-30%) =1.8 liters

Mass of Graphene = 90.90gms

SDBS = 9.090gms (10% of mp)

Ammonium hydroxide = 30 ml (5% of VBF)

Table 2. Net mass of graphene nanoparticles added for different loading

Iteration No.	Actual mass calculated (gms)	Net mass added (gms)
I	9.009	9.009
II	45.22	45.22-9.009 = 36.21
III	90.90	45.68

3.2. Synthesis of nanoparticles

FT-IR (Fourier Transform Infrared Spectroscopy) analysis of the prepared nanoparticle sample

The FT-IR spectrum of the produced sample of a nanoparticle was recorded in the wavenumber interval of 4000-400 cm^{-1}, as shown in figure 2. The spectrum also provides information on surface functional groups of the nanoparticles and supports successful preparation of the intended material.

A clear absorption band at 2921cm^{-1} at 2921cm^{-1} is the stretching vibrations of the aliphatic C5H bonds, which shows the presence of organic or surface-bound stabilizing agents. The absorption peak at almost 1406 cm^{-1} can be explained by C-H bending or C-O stretching vibration indicating the existence of some residual organic functional groups that can stabilize nanoparticles.

Moreover, the presence of characteristic peaks in the lower wavenumber (especially the ones at 1049 cm^{-1} and 767 cm^{-1}) is linked to the presence of metal-oxygen (M-O) stretching vibrations. These peaks confirm nanoparticle formation and indicate a strong affinity for the inorganic lattice. These bands confirm that nanoparticles with well-defined chemical bonds have been successfully synthesized.

The appearance of organic functional groups and co-existence of the inorganic metal-oxygen bonds in the FT-IR spectrum attest to the successful synthesis of nanoparticles and their surface modification. These surface characteristics enhance dispersion stability and functional and thermal performance in subsequent applications.

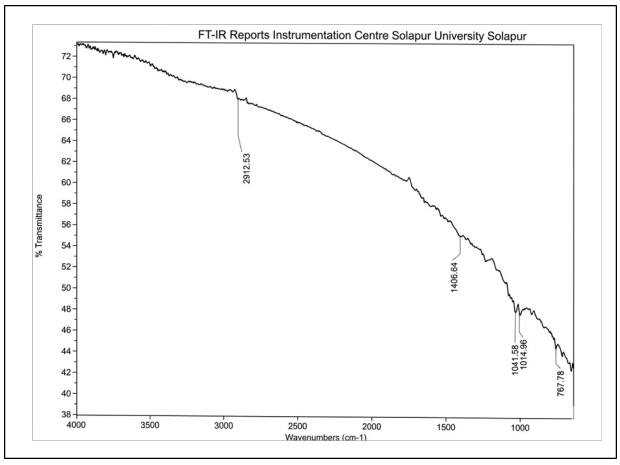

Figure 2. FT-IR spectrum of the prepared nanoparticle sample

3.2.1. FT-IR analysis of the prepared nanoparticles

Figure 2 shows the FT-IR spectrum of the prepared graphene-based nanoparticle sample. The spectrum was measured at wavenumber range of 4000-700 cm^{-1} to determine the functional groups that existed on the surface of the nanoparticle.

The higher wavenumber (around 32003500 cm) absorption at higher wavenumbers is shown in a broad absorption band.

It is proportional to the O-H stretch vibration, which can be explained by the existence of hydroxyl groups and adsorbed moisture on the surface of the graphene. The highest peak at approximately 2921 cm^{-1} corresponds to C-H stretching vibrations, which also suggests the presence of hydrocarbon groups that may have been left over during synthesis or processing.

The other prominent peak, at approximately 1406 cm^{-1}, can be attributed to C=C skeletal vibrations in the aromatic graphene structure. This peak is typical of carbon networks that are sp2-hybridized found in graphene-based materials. At lower wavenumbers, two peaks are observed at around 1046 cm^{-1} and 1014 cm^{-1}, corresponding to C-O stretching vibrations and indicating the presence on the graphene surface of oxygen-containing functional groups such as epoxy or alkoxy groups.

A smaller absorption band at 767 cm^{-1}, attributed to out-of-plane bending vibrations of aromatic C–H bonds, also indicates the presence of graphitic carbon structures.

Graphene-based materials mainly display carbon-based vibrational modes; hence, the FT-IR peaks represent the C-C, C-O, C = C, and O H functional groups rather than metal-oxygen interactions. Such functional groups are frequently found in graphene-based nanomaterials and can promote dispersion and interfacial interactions with the underlying fluid.

3.2.2. Raman spectroscopy analysis

The structure of the graphene nanoparticles was further investigated using Raman spectroscopy. In a typical Raman spectrum, two sharp peaks, the D and G bands, are visible at around 1350 cm^{-1} and 1580 cm^{-1}, respectively.

The G band corresponds to the in-plane vibration of carbon atoms in the graphene lattice, which have two sp2 bonds, and indicates a graphitic structure. The D band is associated with structural defects and disorder in the carbon lattice, which can arise from edge defects, vacancies, or functionalization of graphene sheets.

The intensity ratio of these peaks (I_D/I_G) is commonly used to assess graphene-based materials. In the present study, the calculated I_D/I_G ratio was approximately 0.92, indicating the presence of a moderately defective graphene structure. Such a defect level is generally beneficial for nanofluid applications because surface functional groups improve the dispersion stability of nanoparticles in the base fluid.

3. 2.3. Nanofluid stability

The stability of the prepared graphene nanofluid was assessed prior to the boiling experiments. To ensure uniform dispersion of nanoparticles in the base fluid, the nanofluid was prepared by ultrasonic agitation for about 60 minutes.

The nanofluid was prepared and visually monitored for sedimentation over time. No evidence of settling or agglomeration of particles was observed after approximately 48 hours, indicating that the dispersion remained stable throughout the experimental period. All pool boiling experiments have been carried out under these stable conditions.

3.3. X-Ray Diffraction (XRD) of the nanoparticles synthesized

Figure 3 represents the X-ray diffraction (XRD) pattern of the synthesized nanoparticle sample recorded at various 2θ values from 10 to 80. The crystalline nature, phase purity, and structural aspects of the synthesized nanoparticles were investigated through XRD analysis.

The diffraction pattern is sharp and intense, with a distinct peak at approximately 2θ = 26.3600, which corresponds to the characteristic plane of the crystal. This apex exhibits a well-layered structure and crystalline, synthesized nanoparticles. The sharpness and intensity of this peak show that the crystallites are large and the layers of atoms are arranged regularly.

Other diffraction spots at 2nd of approximately 37.29, 38.60, 39.43 and 42.12 might be due to higher order of reflection or smaller structural planes, which again encourage the existence of a crystalline phase. The purity of the synthesized material is demonstrated by the absence of unwanted or impurity-related peaks in the XRD pattern. In addition, broadened diffraction peaks are a distinguishing feature of nanostructured materials and indicate the nanoscale size of the particles. The smaller crystallite size also increases the surface area; therefore, the nanoparticles are suitable for applications requiring improved thermal and functional performance.

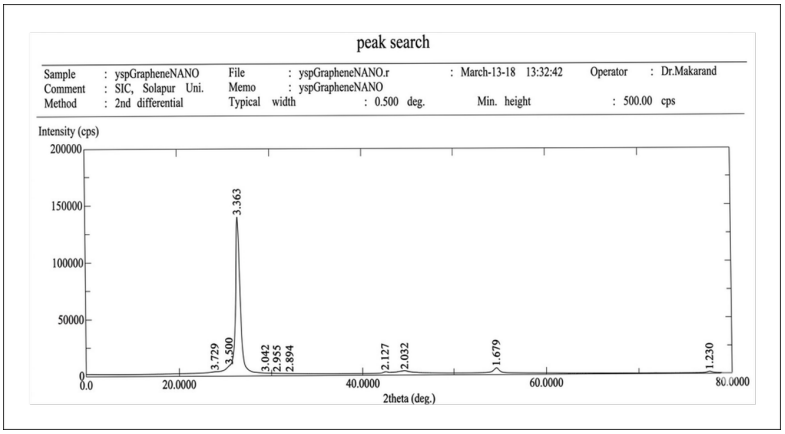

Figure 3. X-Ray Diffraction (XRD) pattern of the synthesized nanoparticles X

RD results confirm the successful synthesis of crystalline nanoparticles with a well-defined crystal structure, indicating their suitability for subsequent experiments and practical studies.

Calculation for size of nanoparticles from XRD results:

Data on the XRD pattern and the Scherrer equation are used to determine the crystallite size of the nanoparticle.

$$d = \frac{C\lambda}{B \cos \theta} \quad (2)$$

where

β = Full width at half maximum of X-ray peak, radians

d = Crystalline size, nm

λ = X-ray wavelength

C = Correction factor

Procedure to calculate crystalline size from graph 2θ =26.48^0

θ =13.24^0

Width(w)= 0.482

Correction factor(C) = 0.9

λ= 1.54056 Å

λ= 0.154056 nm

$$\beta = w \times \frac{\pi}{180} = 8.412 \times 10^{-3}$$

$$d = \frac{C\lambda}{B \cos \theta} = \frac{0.9 \times 0.154056}{0.008412 \times \cos 13.24} = 16.93\text{mm} \approx 17\text{mm}$$

Table 3. XRD-based crystallite size calculation of graphene powder

Sample	β	2θ	θ	cosθ	C	λ	C λ	Bcosθ	Size
Graphene	0.008412	26.48°	13.24°	0.9734	0.9	0.1540	0.1386	0.00818	16.9

3.4. Scanning Electron Microscopy (SEM) analysis of the synthesized nanoparticles

The scanning electron microscopy (SEM) images of the synthesized nanoparticles at various magnifications are presented in Figure 4. SEM was used to analyze the surface morphology, distribution, and structure of the prepared material.

This is reflected in micrographs of a layered, sheet-like morphology that lacks regular, thick flakes of irregular shapes superimposed on each other. The successful creation of the nanosheets, exhibiting a wrinkled, exfoliated morphology, is illustrated by these stratifications. The eventual presence of overlapping sheets and folded edges suggests that there are weak interactions between the layers is a typical aspect of nanomaterials composed of graphene or layers.

At increased magnification, the nanoparticles exhibit rough, uneven surfaces with visible inter-sheet gaps and voids. These morphological features provide it with increased surface area in contact with base fluids and enhanced thermal transport. There are no large agglomerates, indicating that the nanoparticles are uniformly distributed and that the synthesis process was successful.

Moreover, the nanoscale thickness of the sheets and the disordered arrangement promote the formation of a porous structure. This morphology is beneficial for operations that require improved heat transfer, surface activity, and stability.

The SEM analysis has established that the fabricated nanoparticles possess a well-defined, layered nanostructure, have rough surfaces, and are highly dispersible; therefore, they can be used in further experimental work.

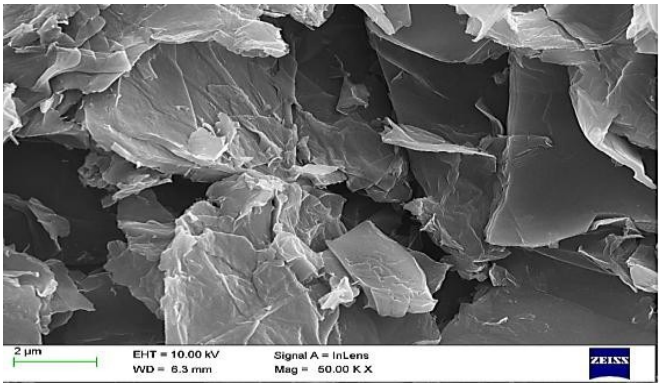

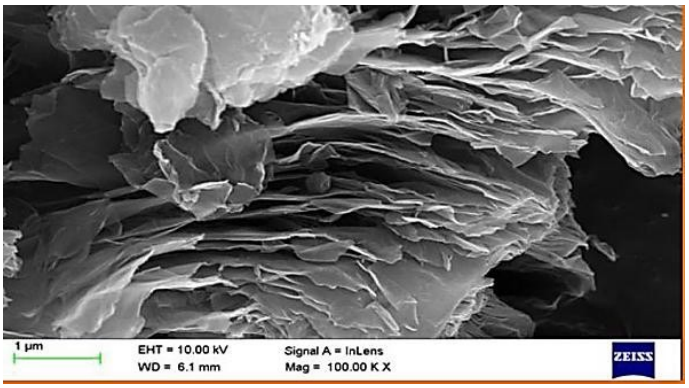

Figure 4. SEM micrograph of the synthesized nanoparticles

3.5. Raman shift

The Raman spectrum of the obtained graphene nanoparticles synthesized was observed in the range of 800 to 4000 cm^{-1}light and is shown in figure 5. Raman spectroscopy is a powerful, non-destructive method for determining the structural quality, the level of disorder, and the number of graphene layers present in carbon nanomaterials.

The spectrum exhibits three characteristic peaks associated with graphene. The D band which is seen at around 1350 cm^{-1} is related to structural defects, edge states and disorder of the graphene lattice. The appearance of such a band indicates defects and finite-size graphene domains, which often arise during nanoparticle synthesis and exfoliation.

The highest peak, the so-called G band, is found at about 1580 cm^{-1}. The sharpness and intensity of the G band confirm the formation of graphitic carbon exhibiting a well-ordered hexagonal lattice.

Also, the 2D band is positioned close to 2700cm^{-1} and is a result of a second-order two-phonon scattering and is very sensitive to the amount of graphene layers. The presence of a distinct, symmetric 2D peak indicates the formation of few-layer graphene rather than of bulk graphite.

The D/G band intensity (ID/IG) provides an estimate of the number of defects in graphene. The average ID/IG ratio in the spectrum indicates a controlled number of defects, which can enhance surface activity and improve interactions with the surrounding medium.

Overall, Raman analysis indicates that the synthesis of graphene nanoparticles - characterized by a predominantly graphitic structure, moderate defect density, and a few layers - was successful, and that the nanoparticles are suitable for subsequent thermal and functional applications.

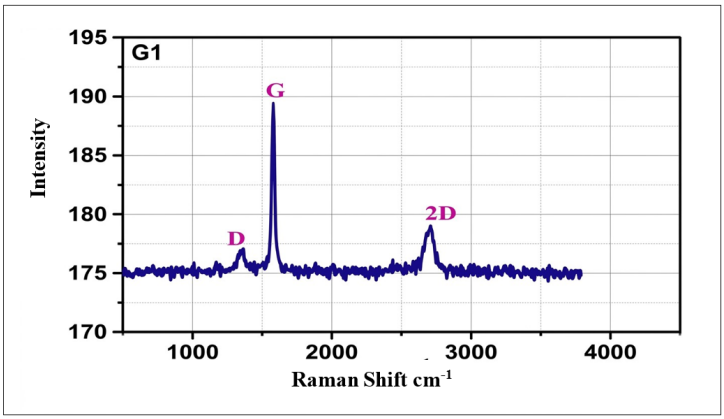

Figure 5. Raman spectrum of graphene nanoparticles

4. Step-wise preparation of graphene nanofluid

Step 1: Nanoparticles selection.

Graphene nano powder is commercially produced by Platonic Nanotech Pvt. Ltd., Jharkhand, India, and was used to make the nanofluid.

Step 2: preparation of base fluid.

The base fluid was prepared by mixing deionized water (DI)and ethylene glycol (EG)in a volumetric ratio of 70:30 and mixed well and then nanoparticles were added.

Step 3: Addition of nanoparticles

The required volumes of graphene nanoparticles were added to achieve volume concentrations of 0.2, 0.5, and 1 in the base fluid.

Step 4: Magnetic stirring

The suspension was stirred in constant magnetic fields to attain primary dispersion of the nanoparticles in the base fluid.

Step 5: Ultrasonication

Ultrasonication was applied to the mixture (30 minutes) to ensure that the dispersion was neither agglomerated with particles nor that they agglomerated.

Step 6: Surfactant addition.

Graphene is hydrophobic, and its dispersion in polar solvents is poor; therefore, the surfactant Sodium Dodecyl Sulfate (SDS) was added. The volume of the surfactant was maintained at 10 percent of the mass of the nanoparticles to improve the stability of the suspension.

Step 7: Determining pH and pH correction

The pH of the nanofluid prior to the introduction of the nanoparticles was 5.5-5.7. To stabilize dispersion, ammonium hydroxide was added to raise the pH. The pH of the nanofluid was adjusted to 8.7-8.9. Step 8: Final Preparation of Nanofluids.

Nanofluids at various volume concentrations were prepared, sealed, and stored under controlled conditions for subsequent thermal and other experimental analyses.

5. Stability of nanofluid

The stability of colloidal suspension can be measured effectively using UV-visible spectrophotometric analysis, which is an easy and effective assessment method. The light absorbance ratio index can be calculated from the absorbance data using the Beer–Lambert law as follows:

$$A = \log \frac{I}{I_i} = \varepsilon.b.c \quad (3)$$

The equation implies that at a given optical path length and molar absorptivity, absorbance is directly proportional to the weight percentage of particles in the suspension. The UV-visible absorption spectrum of the graphene suspension in deionized water exhibits no distinct peaks, and its absorbance gradually decreases with increasing wavelength, except below 250 nm, where a clear absorption band is observed. This absorption band increases with graphene concentration.

Moreover, absorbance decreases as the graphene volume fraction is reduced (e.g., from 1 percent to 0.2 percent). The increasing volume fraction leads to an increase in the absorbance, which is an indicator of the improved dispersion of graphene in the nanofluid. The wavelength (lambda max) at which the absorption is greatest (235 nm), as shown in the figure, implies that the graphene nanofluids are stable. The relationship between absorbance and graphene concentration indicates that the Beer-Lambert law is obeyed and suggests that graphene is stable and well dispersed in the base fluid. GRAPHENE-based NANOFLUID UVVIS Spectroscopic Analysis.

The UV-Visible absorption spectrum of a graphene-based nanofluid at a 1 percent volume fraction over the wavelength range 200-700nm was plotted, as illustrated in Figure 6. UV-visible spectroscopy was employed to characterize the optical properties and dispersion dynamics of graphene nanoparticles in the base fluid.

The absorption spectrum is characterized by a strong peak in the ultraviolet region, with a maximum absorbance at 250-270 nm. The presence of this peak indicates that graphene nanoparticles have been successfully dispersed in the base fluid.

In the extended UV region, the absorbance progressively decreases as the wavelength increases, but the absorbance is not much higher in the visible region. This phenomenon indicates low light-scattering, implying that the nanofluid exhibits strong dispersion stability and that the particles are not agglomerated. The lack of any other sharp peaks indicates that there are no major impurities or secondary phases in the suspension.

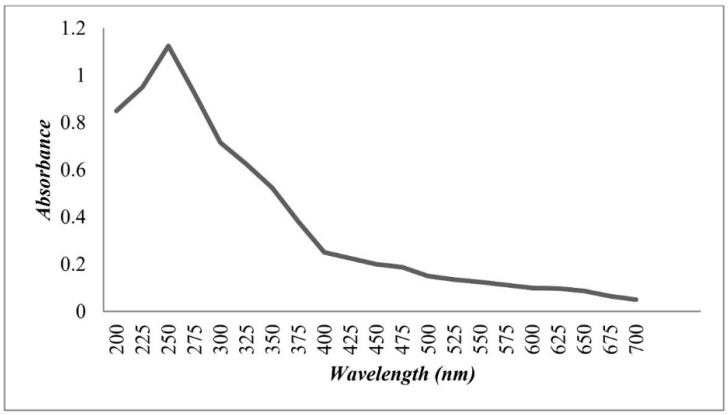

Figure 6. UV–visible absorption spectrum of graphene-based nanofluid at 1% volume fraction

The UV–visible absorption data indicate successful preparation and stable dispersion of graphene nanoparticles in the nanofluid. This optical behavior is desirable in thermal applications because homogeneous dispersion enhances heat-transfer performance.

6. Experimental setup

This study evaluated the heat-transfer performance of different structured heating surfaces under controlled pool-boiling conditions. To this end, a dedicated experimental workshop was painstakingly constructed. The technical requirements of the setup design included the choice of materials, dimensional precision, thermal stability, and assembly. The experimental design enables the precise determination of the heat transfer rate and heat transfer coefficient for various surface geometries. The schematic diagram of the experimental setup is shown in Figure 7.

The system of the experiment is composed of two large subsystems:

i. the boiling chamber and the heater rod assembly.
ii. the electrical measure and control unit.

The heater rod assembly comprises a hollow copper rod, a copper coupler, a structured copper test surface, and a cylindrical electric heater. The electric heater, the primary source of heat, is contained in the hollow copper rod. Heat produced by the heater is transferred to the upper test surface and carried axially along the copper rod. A leak-free connection to the test surface is achieved by permanently welding the copper coupler to the rod and by machining the coupler with internal BSW threads. Interchangeable plain, V-structured, and square-structured copper surfaces are fitted to the coupler, allowing comparisons under the same operating conditions.

To promote primarily one-dimensional heat convection to the test surface and to reduce undesirable heat losses, the heater assembly is insulated with Teflon. The radial and downward heat dissipation are greatly reduced by such insulation, thereby improving the accuracy of heat transfer measurements.

The boiling chamber assembly comprises a bottom flange, a borosilicate glass cylinder, and a top flange. These flanges are made of mild steel, which gives it mechanical strength and a proper seal for the glass chamber. The bottom flange also includes an auxiliary heater, which ensures uniform thermal conditions in the boiling chamber. A borosilicate glass cylinder is selected because it is chemically inert, has a low rate of thermal expansion, and has high thermal shock resistance, which allows safe observation of the boiling phenomenon. All junctions are sealed with silicone sealants to ensure leak-proof performance.

The top flange is equipped with a condenser coil to maintain constant pressure within the boiling chamber and to prevent vapor loss. The generated vapor was condensed by cold water and this allows the operations to be done in closed system with constant pressure in the experiments.

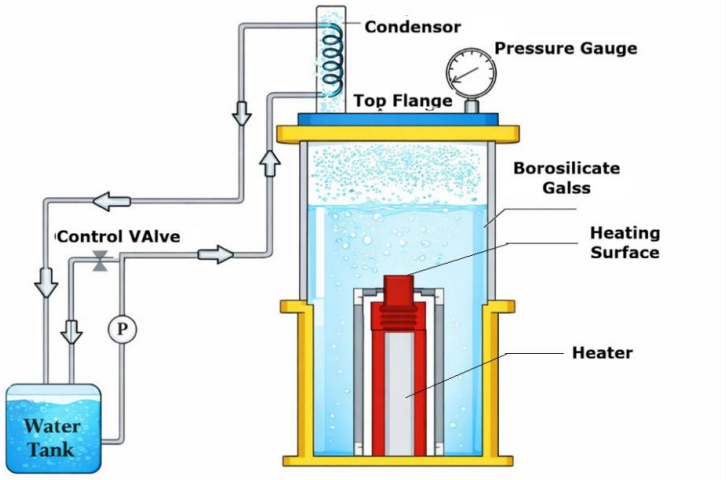

Figure 7. Schematic representation for the experimental setup

The electrical control panel incorporates all the power supply and measurement requirements necessary for safe, controlled experimentation. It has main and auxiliary heaters, a voltmeter, an ammeter, a dimmerstat to control heat input, three K-type thermocouples connected to digital temperature indicators, and a water circulation

pump with individual ON-OFF switches for each heater and for the pump. The combination of this control system allows one to control the experiment's parameters in detail and to collect reliable data. The electrical control panel incorporates all power supply and measurement requirements for safe, controlled experimentation. It has main and auxiliary heaters, a voltmeter, an ammeter, a dimmerstat to control heat input, three K-type thermocouples connected to digital temperature indicators, and a water circulation pump with individual ON-OFF switches for both heaters and the pump. The combination provided by this control system enables one to control experimental parameters in detail and to collect reliable data. Figures 8–10 show different surface structures.

The pool boiling experiments were performed using a cylindrical copper test specimen with a diameter of 20 mm and a height of 40 mm. During the experiments, only the top circular surface of the specimen was exposed to the boiling liquid, while the remaining surfaces were thermally insulated to reduce heat loss to the surroundings.

To investigate the effect of surface geometry on boiling heat transfer, three surface geometries were prepared: plain, V-grooved, and square-structured surfaces. The square-shaped surface consisted of squares with 2 mm sides, evenly machined into the top heating surface. V-shaped grooves, with an approximate width of 2 mm and a depth of about 1 mm, were formed on the V-grooved surface.

Surface roughness was also considered because it influences bubble nucleation during boiling. The mean surface roughness (Ra) of the polished plain surface was about 0.8-1.2 μm, while the machined structured surfaces exhibited slightly higher roughness values of 1.5-2.5 μm. These values are typical for mechanically machined boiling surfaces and help ensure consistency and reproducibility of the experimental results.

Figures 11, 12, and 13 show the boiling phenomena on various structured surfaces.

Figure 8. Plain surface

Figure 9. V Structured surface

Figure 10. Square structured surface

Figure 11. Boiling phenomena on a plain surface

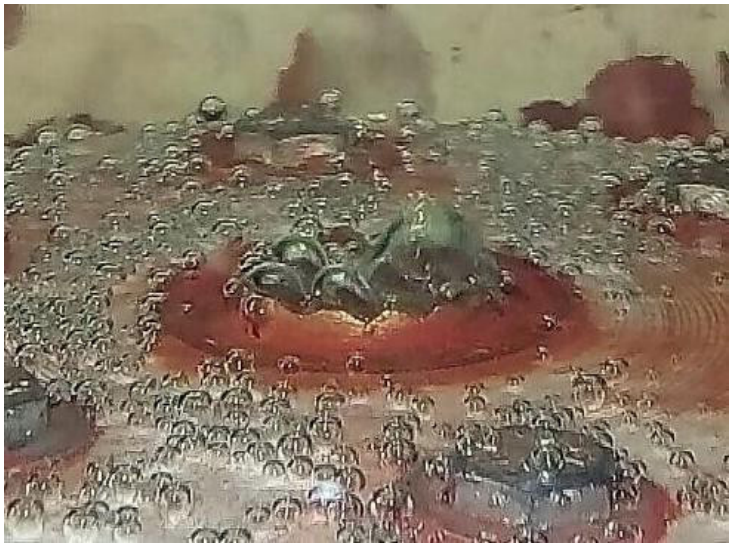

Figure 12. Boiling phenomena on a v-structured surface

Figure 13. Boiling phenomena on a square-structured surface

The boiling process that occurs on the planar surface (Figure 11) is characterized by relatively sparse nucleation sites and the generation of relatively large vapor bubbles prior to departure. The Bubbles have increased the surface residence time and reduced the frequency of departure. This implies that nuclear energy should be restricted to micro-cavities that are naturally present on the smooth surface. The increased bubble diameter causes local thermal resistance due to partial vapor blanketing of the heating surface and limits its efficient rewetting by liquid. Even though the incorporation of graphene nanoparticles improves the effective thermal conductivity and facilitates microlayer evaporation, the lack of ordered geometric features inhibits bubble fragmentation and prevents continuous disruption of the thermal boundary layer. As a result, the heat transfer for the smooth surface is modest.

In contrast, a high density of nucleation sites is evident on the V-structured surface (Figure 12), particularly around the edges and corners of the grooves. The boiling visualization indicates that at the boiling point, the plain surface produces smaller bubbles that detach more frequently than bubbles on the boiling surface. The V-shaped lines can serve as stable entrapment sites for vapor, favoring successive nucleation of geometric discontinuities. Also, the slanted walls facilitate the replenishment of liquids to the heated surface by capillary action. This geometrical restriction lowers the bubble departure diameter and decreases bubble growth time, thereby reducing the formation of vapor blankets. Increased frequency of bubble release disrupts the thermal boundary layer and facilitates surface rewetting. Thus, not only can flow disturbances increase, but geometry-imposed alterations to bubble dynamics and vapor-removal processes can also increase.

The square surface (Figure 13) exhibits the highest boiling activity among all tested configurations. Visualization revealed a high bubble density, multi-site nucleation, coalescence, and immediate bubble detachment. The two square cavities feature several intersecting corners that act as active nucleation sites. These corners enhance the stability of vapor entrapment and substantially increase the number of effective nucleation sites. Geometry also favors bubble division and fragmentation, leading to smaller bubbles and increased departure frequencies. The frequent separation of smaller bubbles further reduces the thickness of the vapor cover and prevents the thermal boundary layer from remaining intact. Increased surface rewetting raises the rate of microlayer evaporation and reduces surface superheat. This explains why the heat transfer coefficient is significantly greater for a square-structured surface.

7. Experimental investigation

Experimentally measured data were used in this study to investigate the system's performance under varying electrical supply conditions, e.g., variations in input voltage and current. Heating surfaces with different structures were tested under steady-state (heating-mode) conditions. Because heat flux is the product of the heat transfer coefficient and the temperature difference between the heating surface and the working fluid, the heat transfer coefficient can be calculated when the temperature difference and the heat flux are known.

To obtain reliable performance comparison in different electrical and thermal conditions, the analysis was done by averaging the 15 successive measurements observed after every 15 minutes in each surface configuration, i.e., the plain surface, V-structured surface and square-structured surface. The average data reduces fluctuations in the experimental data and yields more calculated heat transfer parameters.

Where,

V= Voltage I = Current

T_1, T_2 = Temperature of copper specimen measured at difference in distance is 0.01 m

T_3 = Temperature of nanofluid

7.1. Uncertainty analysis, repeatability and heat loss considerations

To ensure the reliability of the experimental data, repeatability tests and uncertainty analysis were carried out for all measured and calculated parameters. Each experimental condition was tested three times after achieving steady-state operation. The variation observed among repeated measurements was within ±3%, which confirms the good repeatability and stability of the experimental setup. The average values of these repeated measurements were used for the final analysis and discussion.

The uncertainty associated with the experimental measurements primarily arises from the limited accuracy of the measuring instruments. Temperature measurements were obtained using calibrated K-type thermocouples connected to a digital temperature indicator.

±0.5 °C. The electrical input to the heater was determined by measuring voltage and current using digital meters having accuracies of ±0.01 V and ±0.01 A, respectively.

The heat flux supplied to the boiling surface was calculated using the electrical input method:

$$q'' = \frac{VI}{A}$$

where V represents the applied voltage, I denotes the current supplied to the heater, and A is the effective heat transfer area of the heating surface.

The boiling heat transfer coefficient was determined using the relation:

$$h = \frac{q''}{T_s - T_{sat}}$$

where T_s is the measured surface temperature and T_{sat} is the saturation temperature of the working fluid.

The uncertainties in the calculated quantities, such as heat flux and heat transfer coefficient, were estimated by considering the propagation of errors in the primary measured variables. According to the instrument accuracies and calculation process, the uncertainty of the heat flux was in the range of ±5% and the uncertainty in the heat transfer coefficient was in the range of ±7%. The uncertainty levels in pool boiling heat transfer experiments are acceptable.

The loss of heat to the outside world was eliminated by ensuring that the heating assembly was well insulated. As the experiments were performed under steady-state conditions and with insulated boundaries, the heat loss to the surroundings was relatively small. The estimated heat loss was less than 5% of the supplied electrical power; therefore, the electrical input power was assumed to represent the heat transferred to the working fluid with reasonable accuracy.

8. Experimental readings and observations

All experimental readings were recorded under the specified operating conditions. The observations include the measured values of relevant parameters and their corresponding changes during the process. These readings form the primary data for subsequent analysis and interpretation of the experimental results.

Table 4. Experimental readings and observations for plain surface

% of Volume fraction nanoparticles				0.2%			0.5%			1%		
Heat Input	**Sr. No.**	**Current (I)**	**Voltage (V)**	**T_1 (°C)**	**T_2 (°C)**	**T_3 (°C)**	**T_1 (°C)**	**T_2 (°C)**	**T_3 (°C)**	**T_1 (°C)**	**T_2 (°C)**	**T_3 (°C)**
56 W	1	0.7	80	103	102.5	100	103.1	102.4	100.1	102.9	102.1	99.9
	2	0.7	80	103.1	102.7	100.4	102.7	102	99.8	103.2	102.4	99.3
	3	0.7	80	103.3	102.9	100.7	102.5	101.7	100	103.1	102.3	100.1
	4	0.7	80	103	102.5	100.1	103.1	102.4	100	103.4	102.6	100.2
72 W	1	0.8	90	105.1	104.6	99.9	105.1	104.1	99.9	105.3	104.3	100.1
	2	0.8	90	105.6	104.9	100.1	105	103.9	100.1	104.9	103.8	100.3
	3	0.8	90	105.3	104.6	100.4	105.4	104.3	100.5	105.1	104	100.7
	4	0.8	90	105.8	105.2	100.2	105.6	104.5	100	105	104	100.1
90 W	1	0.9	100	107.1	106	101.1	106.9	105.6	100.3	106.8	105.5	99.9
	2	0.9	100	107.4	106.2	100.8	106.8	105.5	100.4	106.9	105.5	100.3
	3	0.9	100	107.9	106.7	100.4	107.5	106.2	100.7	107.4	106	100.5
	4	0.9	100	107.3	106.1	100.1	107.3	105.9	100.1	107.2	105.7	100.8

Table 5. Experimental readings and observations for v- surface

% of Volume fraction nano particles				0.2%			0.5%			1%		
Heat Input	Sr. No.	Current (I)	Voltage (V)	T_1 (°C)	T_2 (°C)	T_3 (°C)	T_1 (°C)	T_2 (°C)	T_3 (°C)	T_1 (°C)	T_2 (°C)	T_3 (°C)
	1	0.7	80	102.1	101.6	100	102.5	101.9	100.1	102.7	102	99.9
56 W	2	0.7	80	102.5	102	100.4	102.8	102.1	99.9	103.1	102.4	100
	3	0.7	80	102.7	102.2	100.7	103	102.4	100	103.4	102.7	99.9
	4	0.7	80	102.3	101.7	100.1	102.3	101.7	100.1	103.2	102.4	100
	1	0.8	90	104.5	103.8	99.9	105.1	104.3	100.5	104.9	104	101.1
72 W	2	0.8	90	104.7	103	100.1	105.5	104.7	100.4	105.1	104.3	100.7
	3	0.8	90	105.1	104.4	100.4	105.8	104.9	100.3	105.3	104.4	100.8
	4	0.8	90	105.3	104.6	100.2	106	105.2	100.5	105.5	104.6	100.9
	1	0.9	100	107.1	106.1	101.1	108	107	100.1	107.5	106.5	99.9
90 W	2	0.9	100	107.3	106.2	100.8	107.5	106.5	99.9	108.1	107	100.5
	3	0.9	100	107.4	106.4	100.4	107.3	106.2	100.1	108	106.9	100.7
	4	0.9	100	107.1	106	100.1	107.7	106.7	100	107.7	106.6	100.1

Table 6. Experimental readings and observations for square surface

% of Volume fraction nanoparticles				0.2%			0.5%			1%		
Heat Input	Sr. No.	Current (I)	Voltage (V)	T_1 (°C)	T_2 (°C)	T_3 (°C)	T_1 (°C)	T_2 (°C)	T_3 (°C)	T_1 (°C)	T_2 (°C)	T_3 (°C)
	1	0.7	80	102.5	101.9	101	103.1	102.3	101.6	102.9	102	101
56 W	2	0.7	80	102.8	102.2	100.9	103.2	102.4	101.1	102.1	102.1	100.9
	3	0.7	80	102.1	101.4	100.8	103	102.1	100.9	103.2	102.1	100.6
	4	0.7	80	102.6	101.9	100.9	103.5	102.6	100.6	103.4	102.3	100.7
	1	0.8	90	105.1	104.3	100.6	105.1	104.1	101	104.9	103.7	100.9
72 W	2	0.8	90	105.3	104.4	100.7	105.6	104.5	100.5	105.3	104	101.1
	3	0.8	90	105.4	104.6	100.8	105.7	104.6	100.8	105.4	104.1	101.6
	4	0.8	90	105.1	104.2	100.5	105.1	104.1	100.7	105.1	103.8	101.1
	1	0.9	100	107.3	106.3	100.9	107.3	106.1	100.6	107.1	105.4	101
	2	0.9	100	107.1	106	100.6	106.9	105.6	100.1	106.9	105.2	100.9
90 W	3	0.9	100	107.5	106.4	100.9	106.8	105.5	100.9	107.2	105.5	100.8
	4	0.9	100	107.4	106.3	101.1	107.1	105.8	100.8	107.3	105.5	100.9

8.3. Calculation of the heat flux and heat transfer coefficient

a) Determination of heat flux (q)

The total electrical heat input supplied to the heating rod is calculated from the measured V and I

$$Q_{input} = V \times I \quad (4)$$

where:

- V= Voltage (V)
- I= Current (A)
- Q_{input}= Electrical heat input (W)

Under steady-state conditions with negligible heat losses (minimized through insulation), the electrical heat input is assumed to be equal to the heat conducted through the test surface.

According to Fourier's law of heat conduction, the heat transfer through the solid surface is:

$$Q = -KA\frac{dt}{dx} \quad (5)$$

Dividing both sides by the heat transfer area (A), the heat flux is obtained as:

$$q = \frac{Q}{A} = -k\frac{dt}{dx} \quad (6)$$

Where,

- q= Heat flux (W/m^2)
- k= Thermal conductivity of the test material (W/m·°C)
- $\frac{dt}{dx}$ = Temperature gradient across the solid (°C/m)
- A= Heat transfer area (m^2)

The temperature gradient (dT/dx) is determined from temperatures measured by embedded thermocouples positioned at known axial distances within the test specimen. For steady-state one-dimensional conduction, a linear temperature distribution is assumed, and the temperature gradient is calculated using the finite-difference approximation:

$$\frac{dT}{dx} = \frac{T_2 - T_1}{\Delta x}$$

where Δx is the known distance between thermocouples.

b) Determination of heat transfer coefficient (h)

The convective heat transfer coefficient is calculated using Newton's law of cooling:

$$q = h(T_s - T_{nf}) \quad (6)$$

Rearranging:

$$h = \frac{q}{(T_s - T_{nf})}$$

where:

h = Heat transfer coefficient ($W/m^2 \cdot °C$)

q = Heat flux (W/m^2)

T_s = Surface temperature of the test specimen (°C)

T_{nf} = Bulk nanofluid temperature (°C)

The surface temperature T_s is determined by extrapolating the linear temperature profile obtained from thermocouple readings to the surface location.

c) Sample calculation procedure

Thermocouples are embedded along the axial direction of the heating rod at a uniform spacing of 0.01 m. The temperatures at these locations are recorded digitally under steady-state conditions.

For example: Distance between thermocouples, Δx = 0.01m Measured temperatures: T_1 and T_2

The temperature gradient is calculated as:

$$\frac{dT}{dx} = \frac{T_2 - T_1}{0.01}$$

Using the known thermal conductivity (k) of the material, the heat flux (q) is calculated from Fourier's law.

The surface temperature is obtained by linearly extrapolating the temperature profile to the outer surface. Finally, the heat transfer coefficient (h) is computed using the measured bulk nanofluid temperature and the calculated heat flux.

9. Results and discussion

This section presents the calculations for the various test surfaces. The surface temperature of each specimen was identified, and the corresponding actual heat transfer rate were identified. Based on the measured temperature differences, the heat transfer coefficient is determined and compared across different surfaces.

9.1. Results and discussion for the plain surface

Tables 4, 5, and 6 show the heat transfer coefficient of a plain surface for different nanoparticle volume fractions.

Table 7. Heat transfer coefficient of a plain surface at 0.2% Nanoparticle volume fraction

Q_{in} [W]	q [W/m^2]	ΔT [^0C]	h [$W/m^2\,^0C$]
56	18.045	1.45	12.45
72	26.22	1.95	13.489
90	47.11	2.705	18.88

Table 8. Heat transfer coefficient of a plain surface at 0.5% Nanoparticle volume fraction

Q_{in} [W]	q [W/m^2]	ΔT [^0C]	h [$W/m^2\,^0C$]
56	32.08	1.925	16.67
72	42.11	2.10	20.07
90	56.14	2.15	26.14

Table 9. Heat transfer coefficient of a plain surface at 1% nanoparticle volume fraction

Q_{in} [W]	q [W/m^2]	ΔT [^0C]	h [$W/m^2\,^0C$]
56	29.07	1.65	17.18
72	43.10	1.73	25.02
90	53.13	1.85	28.19

Figure 14 shows the change in the heat transfer coefficient (h) as a function of heat input (Q_{in}) for nanoparticle volume fractions

of 0.2%, 0.5%, and 1%. At all concentrations, the heat transfer coefficient increases as the heat input increases from 56 W to 90 W, implying increased boiling activity and convective heat transfer at higher thermal loads.

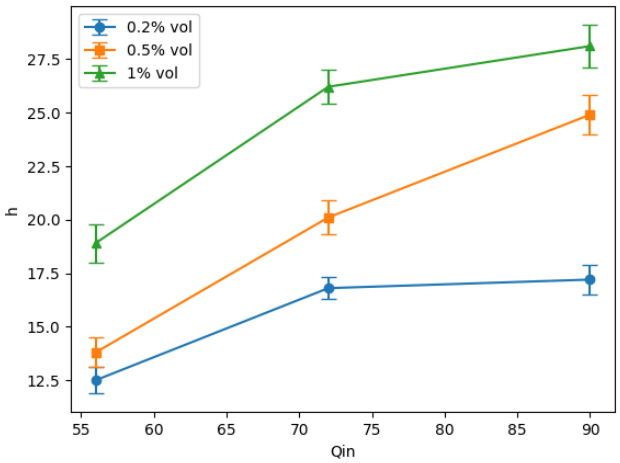

Figure 14. Variation of heat transfer coefficient with heat input for different nanoparticle volume fractions on a plain surface (± standard deviation)

At a given heat input, a high nanoparticle volume fraction results in a high heat transfer coefficient; the 1% nanofluid consistently gives the best performance, followed by the 0.5% and 0.2% nanofluids. This is primarily attributable to the presence of nanoparticles, which enhance thermal conductivity and micro-convection. In general, the findings indicate that heat input and nanoparticle concentration effectively improve heat-transfer performance.

9.3. Results and discussion for the V-structured surface

Tables 7, 8, and 9 show the heat transfer coefficients for a plain surface at different nanoparticle volume fractions.

Table 10. Heat transfer coefficient of a v surface at 0.2% Nanoparticle volume fraction

Q_{in} [W]	q [W/m²]	ΔT [°C]	h [W/m² °C]
56	21.05	1.15	18.30
72	28.07	1.3	21.59
90	39.56	1.425	29.57

Table 11. Heat transfer coefficient of a v surface at 0.5% Nanoparticle volume fraction

Q_{in} [W]	q [W/m²]	ΔT [°C]	h [W/m² °C]
56	25.06	1.025	24.54
72	33.08	1.25	26.54
90	41.10	1.45	28.40

Table 12. Heat transfer coefficient of a v surface at 1% nanoparticle volume fraction

Q_{in} [W]	q [W/m²]	ΔT [°C]	h [W/m² °C]
56	34.24	0.85	34.24
72	36.09	1.0	36.09
90	47.11	1.3	36.145

Figure 15 shows the variation of the heat transfer coefficient with heat input for different nanoparticle volume fractions (V Surface). At three nanoparticle volume fractions (0.2, 0.5 and 1) on the V-structured surface. The heat transfer coefficient increases with heat input (56 W to 90 W) and increasing volume fraction of the mixture, thereby enhancing boiling and overall heat transfer.

An increase in nanoparticle concentration at a fixed heat input increases the heat transfer coefficient. The highest values of h are consistently observed at the 1% volume fraction, followed by 0.5% and 0.2%. That the percentage change in h for the 1-percent nanofluid at higher heat input is more gradual indicates that the V-structured surface already provides considerable flow disturbance and that additional improvement is only moderate. Overall, the findings indicate that increased heat input and increased nanoparticle volume fraction enhance heat transfer on the V-structured surface.

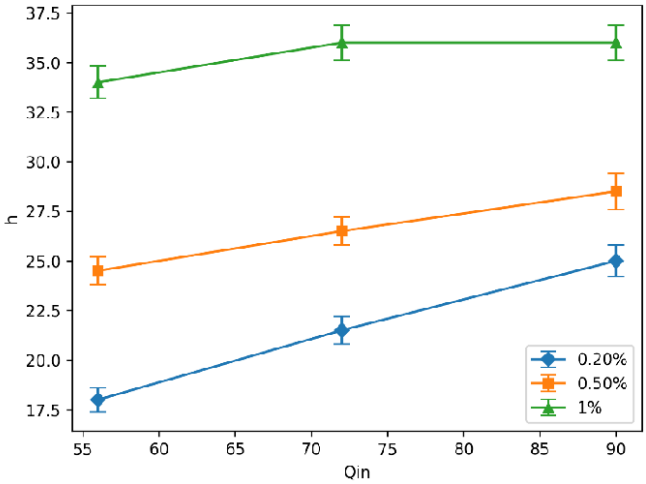

Figure 15. Heat transfer coefficient versus heat input for different nanoparticle volume fractions on v-surface with error bars (± standard deviation)

9.3. Results and discussion for the square-structured surface

Tables 10, 11, and 12 show the heat transfer coefficients on a plain surface across different nanoparticle volume fractions.

Table 13. Heat transfer coefficient of a square surface at 0.2% Nanoparticle volume fraction

Q_{in} [W]	q [W/m²]	ΔT [°C]	h [W/m² °C]
56	26.065	0.85	30.625
72	34.08	1.05	32.81
90	43.10	1.225	35.21

Table 14. Heat transfer coefficient of a square surface at 0.5% Nanoparticle volume fraction

Q_{in} [W]	q [W/m²]	ΔT [°C]	h [W/m² °C]
56	34.08	1.075	31.75
72	42.105	1.15	36.67
90	51.127	1.175	43.80

Table 15. Heat transfer coefficient of a square surface at 1 % nanoparticle volume fraction

Q_{in} [W]	q [W/m²]	ΔT [°C]	h [W/m² °C]
56	41.10	1.15	35.68
72	51.12	1.3	39.32
90	69.17	1.325	52.21

Figure 16 shows how the heat transfer coefficient (h) changes with the heat input (Q_{in}) at various volume fractions (0.2%, 0.5%, and 1%) of the nanoparticles on the square-structured surface. The heat transfer coefficient was found to increase with heat input at all concentrations between 56 W and 90 W, suggesting that boiling activity and heat transfer increase with thermal loading.

The heat transfer coefficient at any given heat input is positively related to the volume fraction of the nanoparticles. The maximum values of h are observed in the 1 percent nanofluid, followed by the 0.5 percent and 0.2 percent nanofluids. The square surface exhibits a faster rate of increase in h with increasing heat input, especially at 1 percent by volume. This can be explained by higher surface roughness, more active nucleation sites, and greater turbulence generation than on plain and V-structured surfaces.

Overall, the findings demonstrate that the square-structured surface, combined with increased nanoparticle concentration, constitutes an effective method for improving heat-transfer performance.

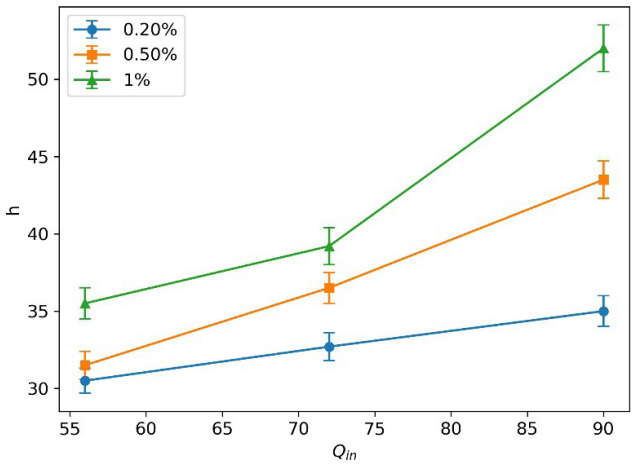

Figure 16. Variation of heat transfer coefficient with heat input for different nanoparticle volume fractions on a square surface with error bar (± standard deviation)

9.4. Results and discussion of different nanofluid volume fractions with various structured surfaces at 90 W heat input

Figure 17 shows the variation in the heat transfer coefficient (h) as a function of nanoparticle volume fraction on plain, V-structured, and square-structured surfaces at a heat input of 90 W. The h of all surfaces increases as the volume fraction increases from 0.2% to 1%, suggesting that a higher nanoparticle concentration improves thermal performance. When the volume fraction is kept constant, structured surfaces outperform the plain surface; the square-structured surface is the most effective with respect to the heat transfer coefficient, followed by the V-structured surface. This pattern confirms that nanoparticle loading and surface geometry enhance heat transfer.

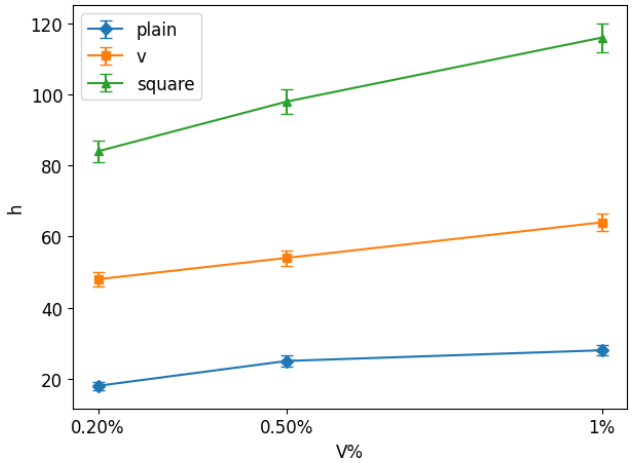

Figure 17. Influence of nanoparticle volume fraction on the heat transfer coefficient for different surface geometries at a heat input of 90 W with error bars(± standard deviation)

9.5. Results and Discussion of Different Nanofluid Volume Fractions with Various Structured Surfaces at 72 W Heat Input

Figure 18 illustrates the influence of the nanoparticle volume fraction (V%) on the heat transfer coefficient (h) of plain, V-structured, and square-structured surfaces at a constant heat input of 72 W. The heat transfer coefficient increases with the volume fraction of nanoparticles (from 0.2% to 1%) across all surface configurations. Structured exhibit higher heat transfer coefficients for a given volume fraction than the plain surface; the square-structured surface shows the greatest improvement, followed by the V-structured surface. This trend indicates that nanoparticle concentration and surface geometry act together to enhance heat-transfer performance under moderate heat input.

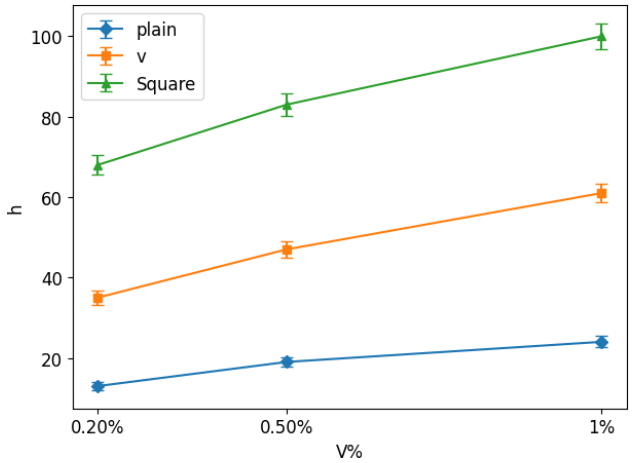

Figure 18. Influence of nanoparticle volume fraction on the heat transfer coefficient for different surface geometries at a heat input of 72 W with error bars(± standard deviation)

9.6. Results and Discussion of Different Nanofluid Volume Fractions with Various Structured Surfaces at 56 W Heat Input

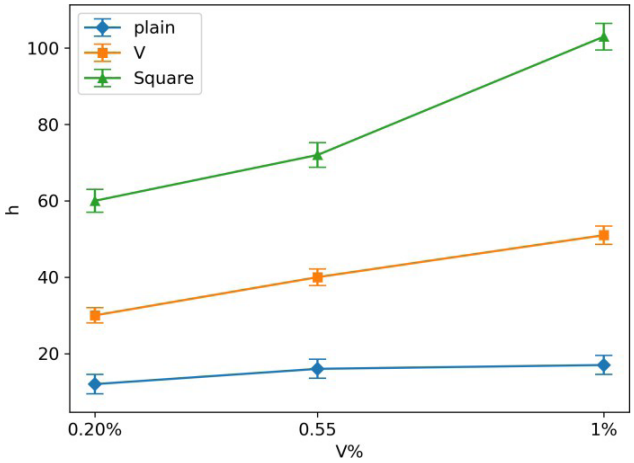

Figure 19. Influence of nanoparticle volume fraction on the heat transfer coefficient for different surface geometries at a heat input of 56 W with error bars (± standard deviation)

Figure 19 shows the heat transfer coefficient (h) as a function of nanoparticle volume fraction (V) for plain, V-structured, and square-structured surfaces at a heat input of 56 W. In all surface configurations, the heat transfer coefficient increases with nanoparticle volume fraction up to 1, indicating improved boiling heat transfer due to increased particle loading.

Structured surfaces are known to have higher heat transfer coefficients than plain surfaces at a constant volume fraction. Among them, the square-shaped surface exhibits the greatest improvement, followed by the V-shaped surface. The observed trend demonstrates the positive synergistic impact of nanoparticle concentration and surface geometry on heat transfer performance, especially under low heat-input conditions.

Various plots of the heat transfer coefficient versus heat input were generated for different surface geometries (plain, V, and square) and volume concentrations (0.2%, 0.5%, and 1%). These plots show improved heat transfer efficiency. The enhancement is determined by heat input and by the volume concentration. One can observe that stable, homogeneous nanofluids can be prepared.

The presence of nanoparticles causes collisions between the heating body and the nanoparticles, which increase turbulence in the solution and, consequently, the heat transfer coefficient.

The appearance of vapor bubbles at the liquid-solid interface during boiling introduces significant thermal resistance. Suspended nanoparticles in nanofluids repeatedly collide with the newly formed vapor bubbles as the bubbles grow on the heated surface. Consequently, vapor bubbles formed in nanoparticle-containing fluids are smaller than those formed in the corresponding base fluids without nanoparticles.

Moreover, a portion of the nanoparticles is likely to be deposited on the heater surface during nucleate boiling, resulting in the formation of a porous layer on the solid-liquid interface. This deposited coating changes the surface properties by altering bubble dynamics, contact angle, and surface roughness. As a result, the wettability of the surface is significantly enhanced, which promotes efficient heat transfer.

When the roughness of the heating surface is several times larger than the nanoparticle diameter, many active nucleation sites become available. This increase in the number of nucleation sites is necessary to promote overall boiling heat transfer.

10. Comparison of all surfaces

The three surface configurations - plain, V-structured, and square-structured, at nanoparticle volume fractions of 0.2, 0.5, and 1% were compared with respect to heat transfer to determine the nature of these surfaces. The evaluation is made on the basis of the experimentally measured heat transfer coefficients at various rates

of heat input, with special focus having been on the combined effect of surface geometry and nanoparticle concentration.

Increasing the nanoparticle volume fraction to 1% produced an overall increase in the heat transfer coefficient across all surface geometries. The nanofluid has superior thermophysical characteristics, including increased effective thermal conductivity and enhanced micro-convection intensity, which increases with nanoparticle concentration. The extent of improvement, however, was quite different with respect to surface geometry.

The plain surface consistently exhibited the lowest heat transfer coefficient across all configurations, volume fractions, and levels of heat input. Although the presence of nanoparticles led to behavioral improvements compared with the base fluid, the absence of surface features inhibited the development of turbulence, as well as access to active sites of nucleation, resulting in only a modest improvement.

By contrast, the V-structured surface exhibited substantially higher heat transfer coefficients than the plain surface at all nanoparticle concentrations. The V-shaped configuration is effective at increasing fluid mixing, disrupting thermal boundary layers, and thereby enhancing heat transfer. However, the rate of improvement declines with increase in heat input which implies that the geometric disturbance caused by V-structure attains a saturation point given some operating conditions.

The square-structured surface was found to be the most effective among the plain and V-structured surfaces across the entire range of the parameter studied (nanoparticle volume fraction). Its geometry produces higher surface roughness and an increased effective area of the active nucleation sites. These properties significantly increase bubble nucleation, departure, and liquid rewetting during boiling, thereby improving heat transfer.

In a comparative analysis of the experimental findings, the square-structured surface exhibited the highest heat transfer coefficient at a heat input of 90 W and a nanoparticle volume fraction of 1%. This condition represents an ideal relationship between surface geometry and nanoparticle loading within the studied range. The notable enhancements in the conditions mentioned above support a strong synergy between graphene-based nanofluids and structured heating surfaces.

Overall, the study confirms that although adding nanoparticles increases heat transfer across all surface types, surface geometry is the dominant factor determining the magnitude of that increase. Among the structures considered, the square-patterned surface provides the best heat transfer performance.

11. Conclusion

The present experimental study explores how nanoparticle volume fraction and surface geometry interact to determine heat-transfer effectiveness as the heat input varies. Nanofluids, consisting of graphene, with volume fractions of 0.2%, 0.5%, and 1%, were applied on plain, V-structured, square structured surfaces at 56 W, 72 W, and 90 W of heat input.

Experimental evidence across all surface geometries, increasing the nanoparticle volume fraction to 1% consistently increases the heat transfer coefficient. This has been mainly due to the favorable thermophysical properties of nanofluids, such as high effective thermal conductivity, intense micro convection, and enhanced energy transport resulting from nanoparticle dispersion. Also, the heat transfer coefficient increased with increasing heat input at a constant nanoparticle concentration, indicating enhanced boiling activity at higher thermal loads.

For a plain surface, the heat transfer coefficient gradually increased with both heat input and nanoparticle concentration. The heat transfer coefficient at 56 W, 25.02 $W/m^{2o}C$, and 28.19 $W/m^{2o}C$ were 23.18, 25.02, and 28.19 respectively at a nanoparticle volume fraction of 1%. These findings support the conclusion that the addition of graphene nanoparticles improves heat transfer even on smooth and unstructured surfaces.

The V-shaped surface consistently exhibited higher heat transfer coefficients than the plain surface under all operating conditions. The values were respectively 34.24 $W/m^{2o}C$ at 56 w, 36.09 $W/m^{2o}C$ at 72 w and 36.15 $W/m^{2o}C$ at 90 w. This has become feasible largely because the V-shaped geometry increases flow disturbance and partially disrupts the thermal boundary layer.

Among all structures tested, the square structure exhibited the greatest heat transfer. The maximum heat transfer coefficient of 56 W was 35.68 $W/m^{2o}C$, 72 W was 39.32 $W/m^{2o}C$, and 90 W was 52.21 $W/m^{2o}C$. The improved performance of this surface can be attributed to increased surface roughness, increased density of active nucleation sites, enhanced turbulence generation and improved liquid–surface contact during boiling.

A comparative evaluation of heat transfer at a nanoparticle volume fraction of 1% and a heat input of 90 W revealed that the V-structured and square-structured surfaces exhibited increases in heat transfer of 28.21% and 85.20%, respectively relative to the unstructured surface. These findings have demonstrated that surface geometry significantly enhances heat transfer, especially when associated with increased nanoparticle concentration.

This paper confirms the hypothesis that the synergistic combination of graphene-based nanofluids and structured heating surfaces can greatly improve the performance of boiling heat transfer. In the studied regime, the square-shaped surface containing a 1% nanoparticle

volume fraction proved the most effective geometry, underscoring its significant potential for application in boiling heat-transfer and thermal-management systems.

Acknowledgement

The authors sincerely acknowledge the valuable support, encouragement, and research facilities provided by Nagesh Karajagi Orchid College of Engineering and Technology, Solapur. The institution's continuous support and the resources made available significantly contributed to the successful execution and completion of this research work.

Author contributions

Suryaji S. Kale: Conceptualization, methodology, experimental investigation, data curation, formal analysis, visualization, writing – original draft preparation, and corresponding author. Sonal S. More: Methodology, validation, data analysis, writing – review and editing, and technical guidance. M. B. Kulkarni, B. R. Birajdar, A. S. Dhobale, and K. A. Shaikh: Contributed to manuscript review, technical discussions, interpretation of results, and critical revision of the manuscript. All authors reviewed and approved the final version of the manuscript.

Conflict of interest

The authors declare that they have no known competing financial interests or personal relationships that could have appeared to influence the research, authorship, or publication of this article.

Data availability

The authors confirm that the data supporting the findings of this study are included within this article. Additional raw data underlying the results presented in this study are available from the corresponding author upon reasonable request.

Declaration of generative AI and AI -assisted technologies in the writing process

The authors declare that no generative artificial intelligence (AI) or AI-assisted technologies were used in the writing, preparation, or editing of this manuscript.

Nomenclature

A	Absorbance
b	Path length, cm
c	Concentration, $mol \cdot L^{-1}$
C	Dimensionless constant related to crystallite shape
d	Crystalline size, nm
DI	Deionized water
dt/dx	Temperature gradient, $°C \cdot m^{-1}$
EG	Ethylene Glycol
FT-IR	Fourier Transform Infrared Spectroscopy
h	Heat transfer coefficient, $W/(m^2 \cdot °C)$
I	Transmitted intensity, W
I_i	Incident intensity, W
K	Thermal conductivity, $W \cdot m^{-1} \cdot °C^{-1}$
M-O	metal-oxygen
mp	Mass of nanoparticles, kg
MWNT	multi-wall nanotubes
q	Heat flux, W/m2
Q	Heat transfer, W
Q_{in}	Heat input, W
SDBS	Sodium dodecyl benzene sulfonate
SEM	Scanning electron microscopy
SWNT	Single-wall nanotubes
SDBS	Sodium Dodecyl Benzene Sulfonate
T	Temperature, °C
UV	Ultraviolet
VBF	Volume of base fluid, m^3
V	Voltage (volts)
I	Current (amp)
XRD	X-ray diffraction
ΔT	Temperature difference, °C

Greek Symbols

β	Full Width at Half Maximum of the diffraction peak (in radians).
E	Molar absorptivity
θ	Half of the diffraction angle (θ = 2θ / 2)
λ	Wavelength of the X-ray source (in nm).
ρ	density of nanoparticles, kg/m3
ϕ	Volume fraction

Subscripts

suf	Surface (Used to indicate surface temperature)
3	Nanofluid (Used to indicate nanofluid temperature)

References

[1] S.U.S. Choi, J.A. Eastman, "Enhancing thermal conductivity of fluids with nanoparticles," Applied Physics Letters, 78 (6) (2001) 718–720. https://doi.org/10.1063/1.1341218

[2] S.K. Das, N. Putra, P. Thiesen, W. Roetzel, "Temperature dependence of thermal conductivity enhancement for nanofluids," Journal of Heat Transfer, 125 (4) (2003) 567–574. https://doi.org/10.1115/1.1571080

[3] D. Wen, Y. Ding, "Experimental investigation into convective heat transfer of nanofluids at the entrance region under laminar flow conditions," International Journal of Heat and Mass Transfer, 47 (24) (2004) 5181–5188. https://doi.org/10.1016/j.ijheatmasstransfer.2004.07.012

[4] P. Keblinski, J.A. Eastman, D.G. Cahill, "Nanofluids for thermal transport," Materials Today, 8 (6) (2005) 36–44. https://doi.org/10.1016/S1369-7021(05)70936-6

[5] S.Z. Heris, M. Nasr Esfahany, S.G. Etemad, "Experimental investigation of convective heat transfer of Al2O3/water nanofluid in circular tube," International Journal of Heat and Fluid Flow, 28 (2) (2007) 203–210. https://doi.org/10.1016/j.ijheatfluidflow.2006.05.001

[6] T.T. Baby, S. Ramaprabhu, "Investigation of thermal and electrical conductivity of graphene-based nanofluids," Journal of Applied Physics, 108 (12) (2010) 124308. https://doi.org/10.1063/1.3516289

[7] W. Yu, H. Xie, X. Wang, X. Wang, "Significant thermal conductivity enhancement for nanofluids containing graphene nanosheets," Physics Letters A, 375 (10) (2011) 1323–1328. https://doi.org/10.1016/j.physleta.2011.01.040

[8] A.A. Balandin, "Thermal properties of graphene and nanostructured carbon materials," Nature Materials, 10 (8) (2011) 569–581. https://doi.org/10.1038/nmat3064.

[9] T.T. Baby, S. Ramaprabhu, "Enhanced convective heat transfer using graphene dispersed nanofluids," Nanoscale Research Letters, 6 (2011) 289. https://doi.org/10.1186/1556-276X-6-289

[10] S.A. Putnam, D.G. Cahill, P.V. Braun, Z. Ge, R.G. Shimmin, "Thermal conductivity of nanoparticle suspensions," Journal of Applied Physics, 99 (8) (2006) 084308. https://doi.org/10.1063/1.2189933

[11] S.G. Kandlikar, "A theoretical model to predict pool boiling CHF incorporating effects of contact angle and orientation," Journal of Heat Transfer, 123 (6) (2001) 1071–1079. https://doi.org/10.1115/1.1409265

[12] A.R. Betz, J. Xu, H. Qiu, D. Attinger, "Do surfaces with mixed hydrophilic and hydrophobic areas enhance pool boiling?" Applied Physics Letters, 97 (14) (2010) 141909. https://doi.org/10.1063/1.3485057

[13] A.R. Betz, J. Jenkins, C.-J. Kim, D. Attinger, "Boiling heat transfer on superhydrophilic, superhydrophobic, and superbiphilic surfaces," International Journal of Heat and Mass Transfer, 57 (2) (2013) 733–741. https://doi.org/10.1016/j.ijheatmasstransfer.2012.10.080

[14] D. Attinger, Z. Yao, D. Poulikakos, et al., "Surface engineering for phase change heat transfer: A review," MRS Energy & Sustainability, 1 (2014) e4. https://doi.org/10.1557/mre.2014.9

[15] C.M. Kruse, T. Anderson, C. Wilson, C. Zuhlke, D. Alexander, G. Gogos, S. Ndao, "Enhanced pool-boiling heat transfer and critical heat flux on femtosecond laser processed stainless steel surfaces," International Journal of Heat and Mass Transfer, 82 (2015) 109–116. https://doi.org/10.1016/j.ijheatmasstransfer.2014.11.023

[16] M. Može, D. Zupančič, I. Golobič, "Laser-Engineered Microcavity Surfaces with a Nanoscale Superhydrophobic Coating for Extreme Boiling Performance," ACS Applied Materials & Interfaces, 12 (19) (2020) 24419–24431. https://doi.org/10.1021/acsami.0c01594

[17] S.W. Ahmad, T.G. Karayiannis, J.S. Lewis, R.J. McGlen, "Pool Boiling on Modified Surfaces Using R-123," Heat Transfer Engineering, 35 (11–12) (2014) 1052–1064. https://doi.org/10.1080/01457632.2014.889493.

[18] [18] Hao Peng, Guoliang Ding "Nucleate pool boiling heat transfer characteristics of refrigerant/oil mixture with diamond nanoparticles" International Journal of Refrigeration 33(2010)347-358

[19] M.A. Kedzierski, M. Gong "Effect of cuO nano lubricant on R134a Pool Boiling heat transfer" International Journal of Refrigeration 32 (2009)791-799

[20] M.A. Kedzierski "Effect of Al2O3 nano lubricant on R134a Pool boiling heat transfer". International Journal of Refrigeration 34(2011)498-508

[21] Saeed Zeinali Heris "Experimental investigation of pool boiling characteristics of low concentrated CuO/ ethylene glycol-water nanofluids" International Communication in Heat and Mass Transfer 38(2011)1470-1473

[22] Adriek suriyawong "Nucleate pool boiling heat transfer characteristics of Ti-O2 water nanofluids at very low concentration" Experimental Thermal and Fluid Science 34(2010)992-999

[23] Pouriya H. Niknam "Numerical Study of low concentration nanofluids pool boiling, investigating of boiling parameters introducing nucleation site density ratio" Heat Mass Transfer (2015) 51:601-609

[24] Sayan sadhu "Heat flux-controlled pool boiling of zirconia-water and silver-water nanofluids on a flat plate: A coupled map lattice simulation" Journal of heat transfer feb-2015 vol.137/ 021503-1a

[25] Visinee trisaksri "Nucleate pool boiling heat transfer of TiO2-R141b nanofluids" International journal of Heat and Mass Transfer 52(2009)1582-1588

[26] Shoji mori "Enhancement of critical heat flux in saturated pool boiling using honeycomb porous media" International Journal of Multiphase Flow 35 (2009) 946-951

[27] Manoj chopkar "Pool boiling heat transfer characteristics of ZrO2-water nanofluids from a flat surface in a pool" Heat Mass Transfer (2008) 44:999-1004

[28] Saeid vafaei "Nanofluid pool boiling heat transfer phenomenon" powder technology 277 (2015) 181-192

[29] Jingliang Bi "Heat transfer characteristics and CHF prediction in nanofluid boiling" International Journal of Heat and Mass Transfer 80(2015)256-265

[30] Yuan –Yang Li "Experimental Study on the saturated pool boiling heat transfer on nano-scale modification surface" International Journal of Heat and Mass Transfer 84 (2015) 550-561

[31] Gengwen Niu "Comparative studies of pool boiling heat transfer with nano-fluids on porous surface" Heat Mass Transfer 00231-015-1542-2

[32] Dawen Zhong "Critical heat flux for downward- facing saturated pool boiling on pin fin surfaces" International Journal of Heat and Mass Transfer 87(2015) 201-211.

[33] J. C. Maxwell, A Treatise on Electricity and Magnetism, 2nd ed., Oxford University Press, Cambridge, 1904, pp. 435–441.
[34] R.L. Hamilton, O.K. Crosser, Thermal conductivity of heterogeneous two-component systems, Ind. Eng. Chem. Fundam. 1(1962)187–191.
[35] Z. Hashin, S. Shtrikman, A variational approach to the theory of effective properties of multiphase materials, J. Appl. Phys. 33(1962)3125–3131.
[36] D.J. Jeffrey, Conduction through a random suspension of spheres, Proc. Phys. Soc., Sect. A 335 (1973) 355–367.
[37] J.D. Jackson, Classical Electrodynamics, 2nd ed., Wiley, London, 1975.
[38] R.H. Davis, Transport of suspended particles at low Reynolds number, Int. J. Theor. Phys. 7 (1986) 609–620.
[39] R.R. Bonnecaze, J.F. Brady, The effective conductivity of random suspensions of spherical particles, Proc. R. Soc. London, Ser. A 432(1991)445–465.
[40] S. Lu, H. Lin, Effective conductivity of composites containing aligned ellipsoidal inclusions of finite length, J. Appl. Phys. 79(1996)6761–6769.
[41] U.S. Choi, Enhancing thermal conductivity of fluids with nanoparticles, in: D.A. Siginer, H.P. Wang(Eds.), Developments and Applications of Non-Newtonian Flows, ASME, New York, 1995, Vol. 231/MD-66, pp. 99–105.
[42] S. Lee, U.S. Choi, S. Li, J.A. Eastman, Measuring thermal conductivity of fluids containing oxide nanoparticles, ASME J. Heat Transfer 121(1999)280–289.
[43] H. Masuda, A. Ebata, K. Teramae, N. Hishinuma, Alteration of thermal conductivity and viscosity of liquid by dispersing ultra-fine particles, Netsu Bussei 4 (1993) 227–233.
[44] H. Akoh, Y. Tsukasaki, S. Yatsuya, A. Tasaki, Magnetic properties of ferromagnetic ultrafine particles, J. Cryst. Growth 45(1978)495–500.
[45] M. Wagener, B.S. Murty, B. Günther, Preparation of metal nanocrystalline powders by cryomilling, in: S. Komarneni et al. (Eds.), Nanocrystalline and Nanocomposite Materials II, MRS, Pittsburgh, PA, 1997, Vol. 457, pp. 149–154.
[46] J.A. Eastman, U.S. Choi, S. Li, L.J. Thompson, S. Lee, Enhanced thermal conductivity through the development of nanofluids, in: S. Komarneni et al. (Eds.), Nanocrystalline and Nanocomposite Materials II, MRS, Pittsburgh, PA, 1997, Vol. 457, pp. 3–11.
[47] J. Kestin, W.A. Wakeham, A contribution to the theory of transport properties of fluids, Physica A 92(1978)102–116.
[48] H.M. Roder, Thermal conductivity measurements at the National Bureau of Standards, J. Res. Natl. Bur. Stand. 86(1981)457–493.
[49] A.I. Johns, A.C. Scott, J.T.R. Watson, D. Ferguson, Thermal conductivity of liquid metals, Philos. Trans. R. Soc. London, Ser. A 325(1988)295–318.
[50] Y. Nagasaka, A. Nagashima, Absolute measurement of thermal conductivity of electrically conducting liquids, J. Phys. E: Sci. Instrum. 14(1981)1435–1440.
[51] Y.S. Touloukian, C.Y. Ho(Eds.),Thermal Properties of Matter: The TPRC Data Series, Vols. 1–13, Plenum Press, New York, 1970–1977.
[52] Du, J., Yang, W., Zhu, H., Wang, J., Cao, Z., Sundén, B., Experimental study of pool boiling performance of Fe_3O_4 nanofluids and nanoparticle deposition surfaces, Applied Thermal Engineering, 240 (2024) 122046.
[53] Freitas, E., Moita, A., Moreira, A., Pool boiling of nanofluids on biphilic surfaces: Bubble dynamics and heat transfer enhancement, Nanomaterials, 11(2021)125.
[54] Moghadam, A.V., et al., Experimental investigation of heat transfer coefficient in pool boiling using hybrid graphene oxide–iron oxide/water nanofluid on grooved surfaces, Case Studies in Thermal Engineering, 2025.
[55] Pereira, J., et al., An overview of recent advances in pool boiling heat transfer enhancement techniques, Micromachines, 15(2024)281.
[56] Ullah, M.Z., et al., Pool boiling enhancement on micro- and nano-structured surfaces: Mechanisms, modeling, and recent advancements, International Journal of Heat and Mass Transfer, 2025.
[57] Abdelrashied, M., Yousery, H., Roshdy, M., Metwally, M., Ali, M., Elsawy, H., Saqr, R., Investigating the effects of nanoparticles and surfactants on heat transfer performance in nucleate pool boiling, International Communications in Heat and Mass Transfer, 2021.
[58] Gupta, S.K., et al., Experimental investigation of hybrid nanofluid boiling heat transfer in structured microchannels, Nuclear Engineering and Design, 2024.
[59] Fadhl, H.H., Enhancement of pool boiling heat transfer using CuO nanofluids on fin-structured heating surfaces, Journal of Sustainable Engineering, 2024.
[60] Kuberan, V., Gedupudi, S., Empirical modeling and machine learning framework for nucleate pool boiling on microchannel structured surfaces, International Journal of Heat and Mass Transfer, 2025.
[61] Sotoudeh, F., Ghazanfarian, J., Molecular dynamics study of surface wettability effects on pool boiling heat transfer over nanoscale aluminum substrates, Physics of Fluids, 2025.
[62] Kale, S. S., & Gawade, S. S. Experimental investigation of convective heat transfer performance using sporadic flow divider type inserts. Journal of Thermal Engineering, 11(2), 331-343. 2025.
[63] Kale, S.S., Gawade, S.S. Heat Transfer Augmentation in Forced Convection with Regularly Spaced Inserts—A Review. In: Pawar, P.M., et al. Techno-Societal 2022. ICATSA 2022. Springer, Cham. 2022.
[64] S. S. Kale, S. S. Gawade and G. Bhosale, "Convective Heat Transfer Enhancement Using Flow Divider Type Insert," 2023 IEEE Engineering Informatics, Melbourne, Australia, pp. 1-5, 2023.
[65] Kale, S. S., & Gawade, S. S. Enhancing Convective Heat Transfer with Bisectional Passive Flow Divider Inserts. International Journal of Basic and Applied Sciences, 14(8), 52-62. 2025.

[66] S. S. Kale, S. S. Gawade and G. Bhosale, "Convective Heat Transfer Enhancement Using Flow Divider Type Insert," 2023 IEEE Engineering Informatics, Melbourne, Australia, pp. 1-5, 2023.